

Ductility-Dip Cracking Susceptibility of Nickel-Based Weld Metals: Part 2 – Microstructural Characterization

Ductility-dip cracking in Ni-Cr-Fe weld metals was attributed to grain boundary sliding in the temperature range from approximately 750° to 1150°C

N. E. NISSLEY AND J. C. LIPPOLD

ABSTRACT

Part 2 of the investigation of the ductility-dip cracking (DDC) susceptibility of Ni-Cr-Fe filler metals describes experiments and characterization designed to provide a better understanding of the DDC mechanism. The strain-to-fracture (STF) DDC susceptibility varied significantly with only minor changes in composition and was influenced by the solidification microstructure. Optical metallography, electron backscatter diffraction (EBSD), thermodynamic calculations, and heat treatments were used to better understand microstructural factors that influenced susceptibility to DDC.

The DDC cracking susceptibility was compared with thermodynamic calculations to better understand how carbide precipitation affects grain boundary sliding and the mechanism for DDC. Macroscopic grain boundary locking occurs in alloys that form interdendritic MC-type carbides at the end of solidification. A significant decrease in the DDC susceptibility was found in alloys with Mo and Nb additions that resulted in a dense distribution of skeletal MC-type carbides. The carbide morphology and distribution affects boundary migration and results in wavy or tortuous grain boundaries that mechanically lock the grain boundaries and oppose the sliding that promotes cracking. Microscopic grain boundary locking occurs in alloys that form intergranular $M_{23}C_6$ carbides. The distribution, morphol-

ogy, and precipitation kinetics of these carbides affect their ability to limit grain boundary sliding.

Solutionizing and subsequent precipitation heat treatment improved the resistance to DDC. This resistance was attributed to microstructure homogenization, and $M_{23}C_6$ precipitation that resulted in reduced grain boundary sliding. In one Filler Metal 52M alloy, the elongated intergranular $M_{23}C_6$ carbides promoted dynamic recrystallization during STF testing that was attributed to particle stimulated nucleation (PSN).

Based on this investigation, DDC in Ni-Cr-Fe weld metals is clearly attributed to grain boundary sliding in the temperature range from approximately 750° to 1150°C. The precipitation of MC-type carbides at the end of solidification results in pinning of the migrated grain boundaries that make these boundaries “tortuous” and resistant to sliding. In addition, the precipitation of $M_{23}C_6$ carbides in the solid state provides additional microscopic locking of the boundaries that further improves resistance to DDC.

Introduction

In Part 1 of this investigation, the ductility-dip cracking (DDC) susceptibility of Ni-Cr-Fe filler metals was evaluated using

KEYWORDS

Ductility Dip Cracking
Nickel-Based Alloys
Precipitation Heat Treatment
Grain Boundary Sliding
Weld Process Simulation
Strain-to-Fracture Testing

N. E. NISSLEY, formerly a graduate research associate at The Ohio State University, is currently with ExxonMobil Upstream Research Co., Houston, Tex. J. C. LIPPOLD is a professor in the Welding Engineering Program at The Ohio State University, Columbus, Ohio.

the strain-to-fracture (STF) Gleeb-based testing technique (Ref. 1). Part 2 of this investigation focuses on the mechanism of DDC in these weld metals. Numerous mechanisms for DDC have been proposed for multiple alloy systems and include sulfur embrittlement (Refs. 2, 3), grain boundary sliding (Refs. 3–7), and $M_{23}C_6$ precipitation-induced cracking (Ref. 8). The lack of consensus on the mechanism for DDC is due to multiple contributing factors that add to the complexity of DDC in different alloy systems. This complexity limits the use of some testing techniques where there are too many uncontrolled variables and limited options for a systematic evaluation. The Gleeb-based STF test has demonstrated significant advantages for assessing DDC susceptibility, including 1) a reproducible starting microstructure, 2) a single testing temperature that isolates the DDC-susceptible temperature field, 3) control of strain at the test temperature, and 4) can be used for both on-heating and on-cooling tests (Refs. 5, 9).

Based on previous research, there is a lack of consensus on the effect of composition on DDC susceptibility. Dix and Savage reported that in Inconel® X-750, carbides appeared to inhibit grain boundary sliding, which improved the ductility, and they found no evidence of embrittlement due to carbide precipitation (Ref. 7). Rhines and Wray reported that grain boundary shearing in Monel® was the cause of the DDC, and boundary orientation was important (Ref. 10). Similarly, Ramirez and Lippold reported evidence of grain boundary sliding in FM-52 and 82 and proposed that it was caused by a creep-like mechanism associated with grain boundary sliding (Refs. 11, 12). Had-drill and Baker reported that in 25-Cr/20-Ni stainless steels, increased carbon reduced DDC susceptibility, and concluded that the cracking could not be caused by strain-induced precipitation (Ref. 13). Arata et al. reported that an increase in carbon reduced cracking in stainless steels

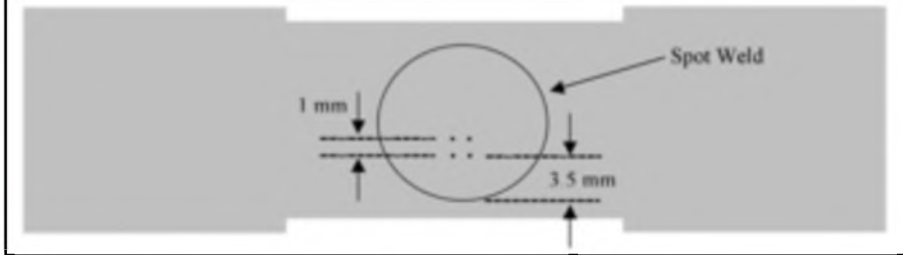


Fig. 1 — Schematic showing the location of the four indentations forming a 1- × 1-mm square inside the spot weld on the STF sample. The indentations were used to locate the same area for EBSD scans before and after STF testing and were located 3.5 mm from the edge of the spot weld. (Not to scale.)

Table 1 — All-Weld-Metal Compositions (wt-%) of the Three Experimental Alloys that Were Further Evaluated

	Mat. B (FM-52M)	Mat. C (FM-52M)	Mat. H (N/A)
Ni	59.54	60.38	53.87
Cr	30.06	29.5	30.18
Fe	8.22	8.04	8.2
Nb	0.83	0.82	2.48
C	0.02	0.03	0.021
Mn	0.80	0.77	0.8
Si	0.001	0.001	0.001
P	0.003	0.004	0.004
Si	0.09	0.12	0.2
Cu	0.02	0.01	—
Al	0.11	0.12	0.04
Ti	0.22	0.19	0.2
Mo	—	—	4
B	0.003	0.001	0.001
Zr	0.01	0.008	0.007

and attributed this to $M_{23}C_6$ carbides restricting grain boundary mobility. However, Young et al. tested a number of Ni-Cr weld metals and concluded that DDC was caused by $M_{23}C_6$ precipitation-induced cracking (Ref. 8). Zhang et al. reported that in Invar®, grain boundary sliding coupled with intergranular precipitates and serrated grain boundaries led to the observed DDC cracking (Ref. 14). Lin and Cola reported strain concentration at grain boundaries of FM-52 weld metal and proposed that the difference in ductility between the grain interiors and boundaries may account for the DDC cracking (Ref. 15).

Collins et al. found that additions of sulfur and/or hydrogen increased the susceptibility to DDC in FM-82 (Refs. 16, 17). Ramirez and Lippold reported that in FM-52 and 82 sulfur affected cracking but bulk sulfur levels were not sufficient to define DDC susceptibility (Ref. 11). Nishimoto et al. reported that in Alloy 690, sulfur and phosphorus had an embrittling effect on grain boundaries but reported a recovery with lanthanum additions (Refs. 3, 18, 19). Capobianco and Hanson proposed that for FM-52, the ductility-dip may be caused by the combined effect of

sulfur embrittlement and local stress from $M_{23}C_6$ carbide precipitation (Ref. 20). Young et al. concluded that DDC in their Ni-Cr alloys was not controlled by grain boundary impurity segregation of sulfur (Ref. 8). In Invar, Matsuda et al. found that sulfur, oxygen, nitrogen, and aluminum promoted DDC while silicon and manganese inhibited DDC (Ref. 21). Nishimoto et al. found that the sulfur embrittlement of grain boundaries in Invar was accelerated by reheating during multipass welding (Ref. 2).

There have been numerous reports where Nb and/or Ti carbonitrides in Ni-based alloys have altered the grain boundary morphology and decreased the DDC susceptibility (Refs. 8, 11, 12, 22–28). This seems consistent with the extensive cracking observed in commercially pure nickel 200 reported in Part 1, which is essentially free of carbides (Ref. 1).

Several authors have reported that in Ni-based alloys the orientation of the boundary and the applied strain affected cracking (Refs. 12, 16, 23, 24, 26) and Kikel and Parker reported that rotating the weld 90 deg to the applied strain reduced DDC (Ref. 23). Davé et al. found that “special” grain boundaries in Alloy 690 were less susceptible to DDC than random boundaries (Ref. 29). Collins et al. observed that DDC only occurred along random, high-angle boundaries (Ref. 24).

Significant heat-to-heat variation continues to be reported, that, based upon our current understanding of the DDC mechanism, could not have been predicted solely by composition (Refs. 16, 25, 28). Additional understanding of the effect of bulk composition on ductility-dip cracking susceptibility is needed to understand and avoid cracking in the future.

Experimental Procedures

In Part 1, eight experimental Ni-Cr-Fe alloys were prepared and tested for DDC susceptibility with the STF test (Ref. 1). Based upon these results, materials B, C, and H (Table 1) were selected for further microstructural evaluation to better un-

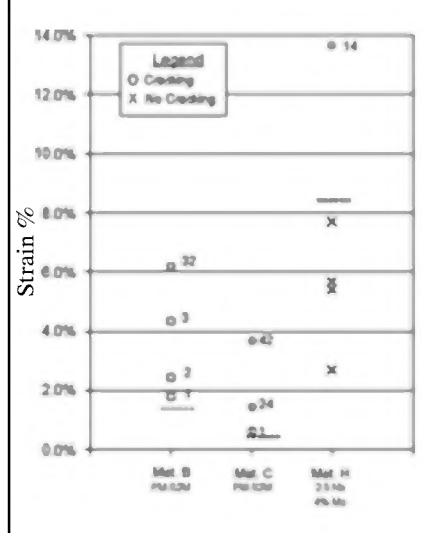


Fig. 2 — STF test results for baseline testing at 950°C for experimental FM-52M compositions. An “x” represents a tested sample with no DDC cracking and an “o” a sample with DDC cracking. The number next to the circle is the number of DDC cracks found in the sample. Materials B and C are experimental heats with the same target composition except for boron, and material H has higher Mo and Nb.

derstand the factors affecting DDC susceptibility. Materials B and C are experimental Filler Metal 52M (FM-52M) alloys and material H is a FM-52M-like alloy with additions of 2.5% Nb and 4% Mo. FM-52M (AWS A5.14, ERNiCrFe-7A) is a second-generation welding wire for joining Alloy 690 in nuclear applications where SCC and DDC resistance are required.

In the present work (Part 2), all of the alloys were evaluated before and after STF testing using optical microscopy, scanning electron microscopy (SEM), and electron backscattered diffraction (EBSD). The microstructural observations were compared with solidification and equilibrium thermodynamic calculations and with the STF testing results. Based upon these observations, samples were heat treated to alter the as-welded carbide distribution and then STF tested to better understand the effect of carbide precipitation on DDC susceptibility.

Microstructural Analysis

Samples prepared for optical and electron microscopy were mechanically polished through 3 μm diamond paste and then electropolished prior to each scan to expose a clean surface. Electropolishing was performed with a Struers LectroPol-5 using Struers A2 polishing solution and developed operating parameters (39 V, $\sim 1.7 \text{ A/cm}^2$, 3 cm^2 mask, 18 flow, 22°C, 15

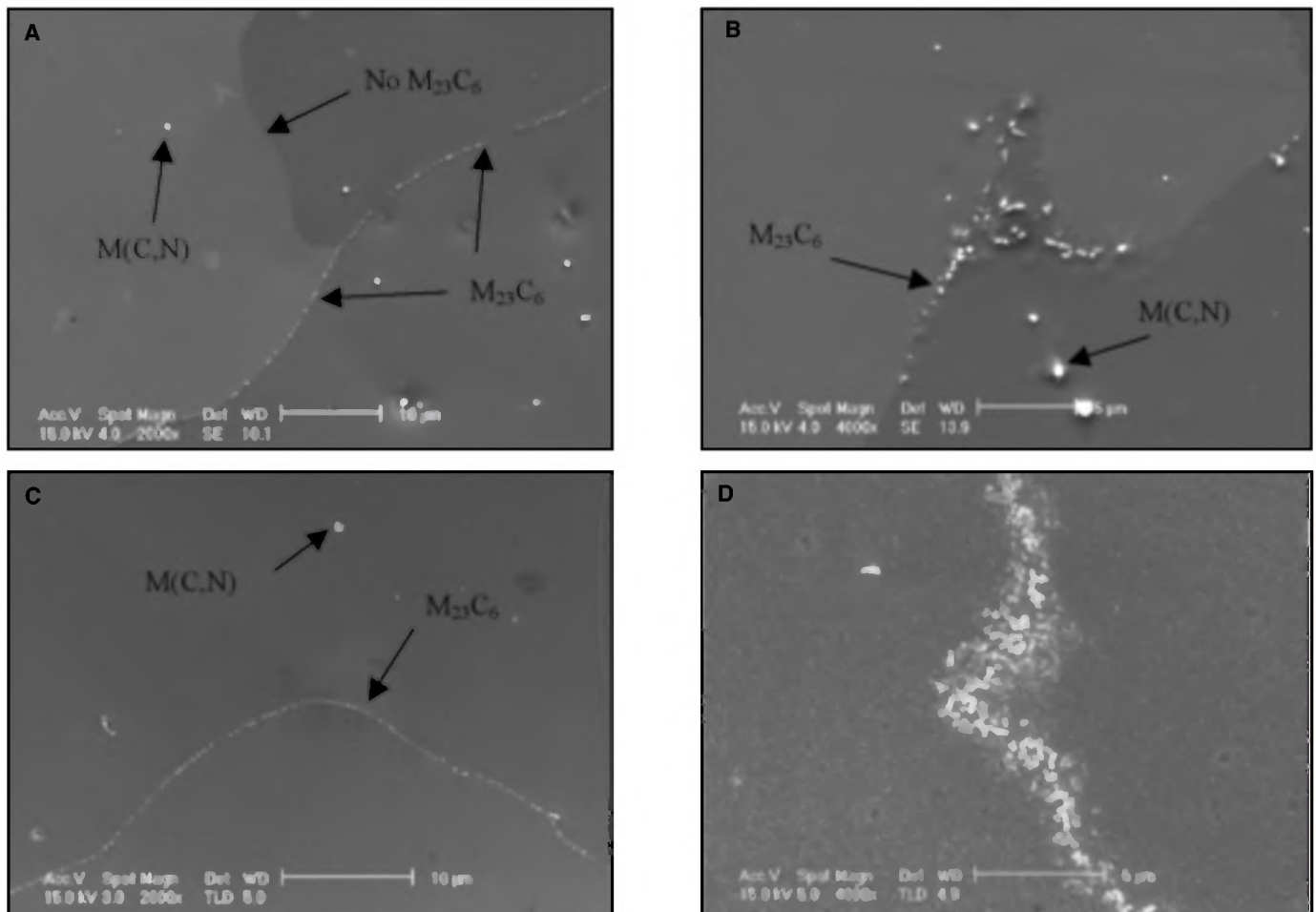


Fig. 3—Material B sample showing the as-welded (spot weld) microstructure (A and B) and the STF tested (950°C) microstructure (C and D). M(C,N) carbides are visible in the interdendritic regions in both cases while the M₂₃C₆ carbides were found on select boundaries as welded and on almost all boundaries after STF testing.

s) (Ref. 5). Electropolishing was found to be beneficial as it produced a deformation-free sample surface required for EBSD but did not etch away the carbides, leaving them exposed above the surface. Samples were etched with a 10% chromic acid solution at 1.5 to 2 V for 30 s when required.

Strain-to-fracture testing was completed on-heating using standard testing procedures detailed in Part 1 (Ref. 1). On-cooling STF tests were not completed during this study due to the additional test variables that are introduced (e.g., peak temperature, cooling rate) and the fact that a significant number of cracks are observed in these alloys on-heating at low levels of strains. Standard STF spot welds with a 12.7-s downslope time were used for all reported data. Samples were heated in the Gleeble to the test temperature, held for 10 s, and strained different amounts. After cooling to room temperature, the strain and number of cracks were determined with the aid of a binocular microscope at magnifications up to 30 X. The results of the test are plotted on a

temperature-strain plot with the number of cracks beside each point. The STF results include the threshold strain and the transition to gross cracking. The threshold strain is defined as the lowest strain over the entire DDC temperature range at which the material begins to crack. While the complete on-heating DDC temperature range was not tested for these alloys due to a limited number of samples, the use of the term threshold strain in this paper is used to describe the minimum strain at which the samples started cracking at 950°C. Other STF tests to date on FM-52 and FM-52M alloys (Refs. 9, 27, 30) have shown that 950°C can provide a reasonable estimate of the threshold strain for these alloys. The transition to “gross” cracking is defined as the strain where cracking becomes so abundant that cracks begin to grow and connect, making accurate crack counting difficult. The gross cracking transition can be defined when the slope of the number of cracks from one sample to the next exceeds approximately 10 cracks per percent strain.

Electron microscopy was performed

with three separate scanning electron microscopes for imaging, EDS chemical analysis, and EBSD (Ref. 31). All SEM imaging and EDS analyses were performed at 15 keV, and EBSD was performed at 25 keV. Quantitative analysis of carbides with the EDS data was limited due to the size of the electron beam interaction volume. The EBSD data collection and analysis was performed with the EDAX TSL OIM™ software.

Deformation

Electron backscattered diffraction was performed before and after STF testing with a modified sample geometry. While the total STF sample length was reduced to 3.75 in. (9.5 cm) to accommodate the space limitations of the EBSD chamber, the gauge length and spot weld remained the same (Ref. 5). After the sample was prepared according to the standard polishing and etching procedure described previously, a set of four Vickers microhardness indentations were made on the sample surface with the use of a microme-

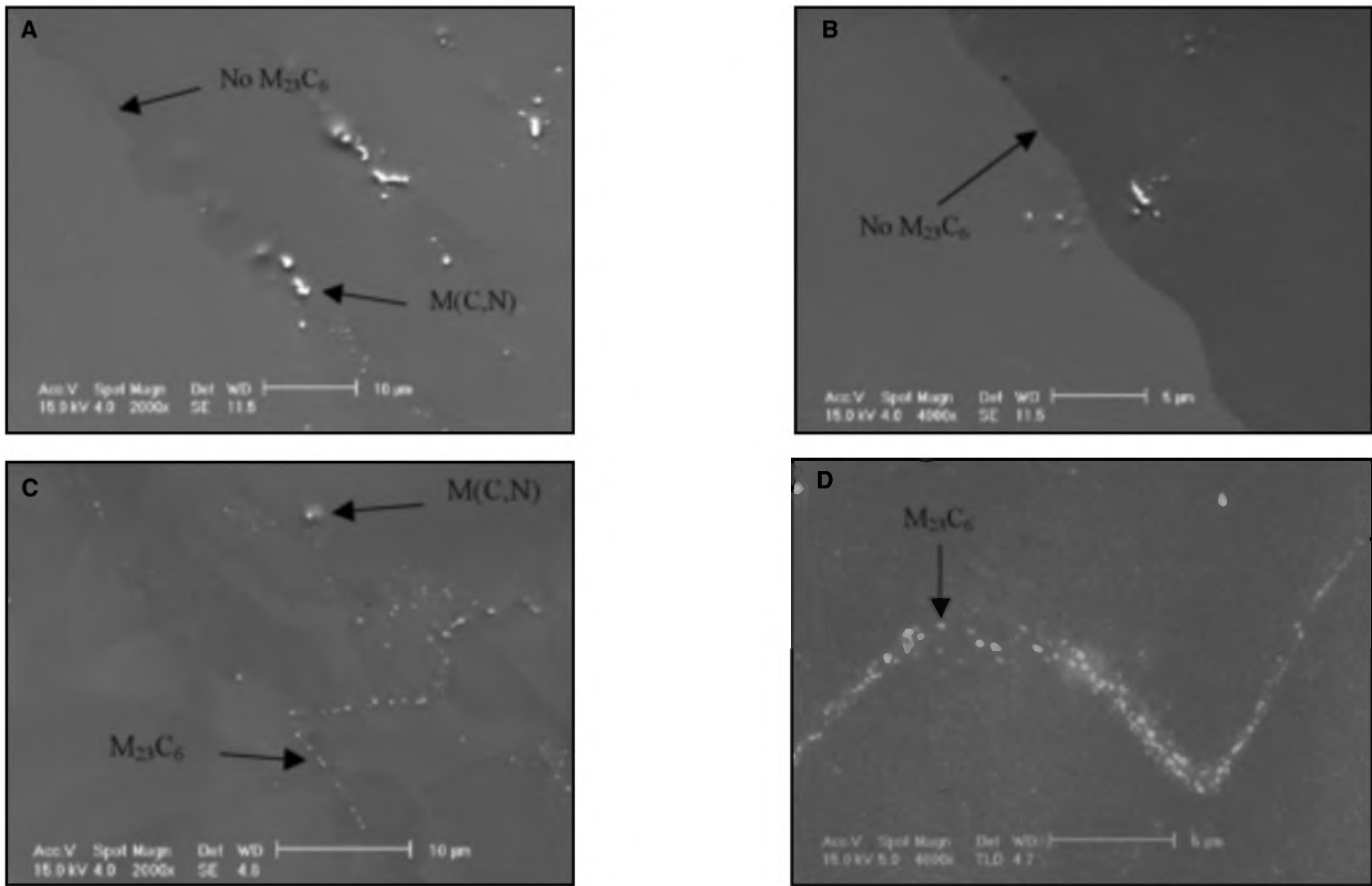


Fig. 4 — Material C sample showing the as-welded (spot weld) microstructure (A and B), and the STF tested (950°C) microstructure (C and D). M(C,N) carbides are visible in the interdendritic regions but no $M_{23}C_6$ carbides were found as welded and only sporadically after STF testing.

ter-controlled stage to form a 1-mm square inside the spot weld. The indentations allowed for the same location to be identified before and after STF testing on the sample in the tilted and polished condition that was required for EBSD — Fig. 1. The spot welds were typically 10 to 11 mm (0.41 to 0.45 in.) in diameter and the four indentations were located 3.5 mm (0.14 in.) from the edge to avoid the elongated columnar grains that formed near the

edge of the spot weld and any abnormality that might exist in the center. The sample was then electropolished for 10 s to remove the etching effects, but leaving evidence of the Vickers indents and allowing for location identification for EBSD. Collected EBSD scans were 0.75-mm (0.3-in.) square with a 2- μ m step size and centered inside the four microhardness indentations. Following the before-STF EBSD scan, the sample was STF tested, electropolished

again for 10 s to remove the thin oxide layer, and then rescanned.

This technique provided information on how the microstructure accommodated the strain during the STF test and gave insight into what effect the starting microstructure had on DDC susceptibility. This technique was successful up to strains of approximately 4%. As the strain exceeded 5%, the amount of surface deformation was sufficient to prevent acquisi-

Table 2 — Results of Microstructural Analysis Compared with JMatPro-Ni v. 7 Thermodynamic Solidification Calculations* for Materials B, C, and H (Ref. 5)

	Material B		Material C		Material H	
	Spot Weld	STF	Spot Weld	STF	Spot Weld	STF
M(C, N)	0.5–2 μ m Fig. 3A Predicted*	0.5–2 μ m Fig. 3B	0.5–2 μ m Fig. 4A Predicted*	0.5–2 μ m Fig. 4B	1–5 μ m Fig. 5A Predicted*	1–5 μ m Fig. 5B
$M_{23}C_6$	Sporadic on GBs <0.5 μ m	Consistent on GBs <0.5 μ m	None Observed	Inconsistent on GBs <0.5 μ m	None Observed	Sporadic on GBs <0.5 μ m
Delta	N/A	N/A	N/A	N/A	Possible Predicted*	Possible
Laves	N/A	N/A	N/A	N/A	Possible Predicted*	Possible
Sigma	N/A	N/A	N/A	N/A	Possible Predicted*	Possible

*Note: "Predicted" indicates that the phase was present in the JMatPro calculations. "Possible" indicates that the EDS methods used were not sufficient to differentiate between the different phases.)

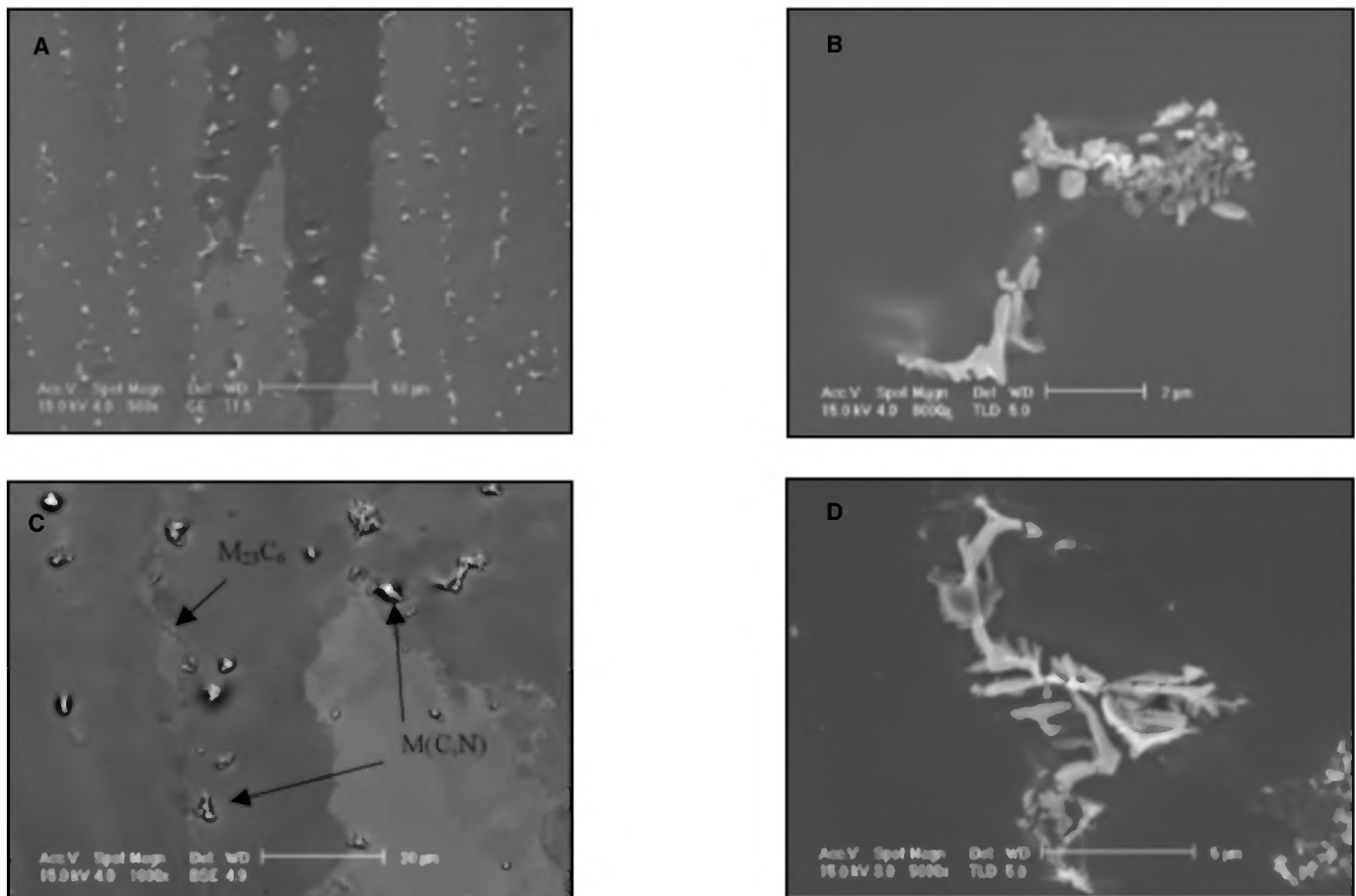


Fig. 5—Material H sample showing the as-welded (spot weld) microstructure (A and B) and the STF tested (950°C) microstructure (C and D). Large M(C,N) carbides are visible in the interdendritic regions that resulted in wavy or tortuous grain boundaries.

tion of the EBSD diffraction pattern on heavily deformed portions of the sample.

Grain reference orientation deviation (GROD) plots were used to evaluate orientation differences within individual grains. The average orientation within a given grain was calculated and all points within the grain with the same orientation as the average were colored blue (0-deg deviation). As the angular deviation of the points increased from the average orientation, the color transitioned through green, yellow, orange, and red (16-deg deviation). The before and after GROD plots are insightful when evaluating how deformation is accommodated within a material. Additional information on the EBSD and GROD procedure can be found elsewhere (Ref. 5).

Carbide Engineering

JMatPro-Ni v. 7 by Thermotech Ltd. was used for all thermodynamic calculations. The nickel database included the following elements: Ni, Al, Co, Cr, Cu, Fe, Hf, Mn, Mo, Nb, Ru, Re, Si, Ta, Ti, V, W, Zr, B, C, N, and O. Any elements not listed

in Table 1 were not used in the calculation except nitrogen, which was assumed to be 0.002 wt-%. Three primary types of calculations were performed: stable and metastable phases, solidification, and phase transformation (CCT/TTT) calculations (Ref. 5).

Sample heat treatment prior to STF testing was conducted with the Gleebel to alter the carbide type, size, distribution, and morphology. Samples were prepared using the same procedures used for STF testing but no mechanical force applied during heating. A solution annealing heat treatment at 1275°C for 1 min was used in conjunction with $M_{23}C_6$ carbide precipitation heat treatments at 700°C for 5 and 3.75 h for materials B and C, respectively. These temperatures and hold times were based upon thermodynamic calculations using JMatPro-Ni v. 7. The precipitation heat treatment temperature was selected to minimize grain growth while keeping the heat treatment times reasonable. Samples were heated to temperature at 100°C/s and afterward were allowed to free cool to room temperature without any external mechanical loading.

Results and Discussion

Based upon the STF results of Part 1 (Ref. 1), materials B, C, and H were selected for further evaluation to provide additional insight into the DDC mechanism. While both materials B and C had similar compositions (with the exception of a small difference in boron content), their DDC resistance varied significantly — Fig. 2. While both alloys cracked at relatively low threshold strains (< 1.5%), the additional strain required to transition to gross cracking varied significantly. Material B transitioned to gross cracking above 5% while material C transitioned around 1.5% strain. Material H was selected due to its high threshold strain (~8%) and general resistance to gross cracking (>14% strain).

Microstructural Analysis

Microstructural analysis was performed before and after STF testing on materials B, C, and H to better understand the effect of the microstructural evolution and carbide morphology on DDC suscep-

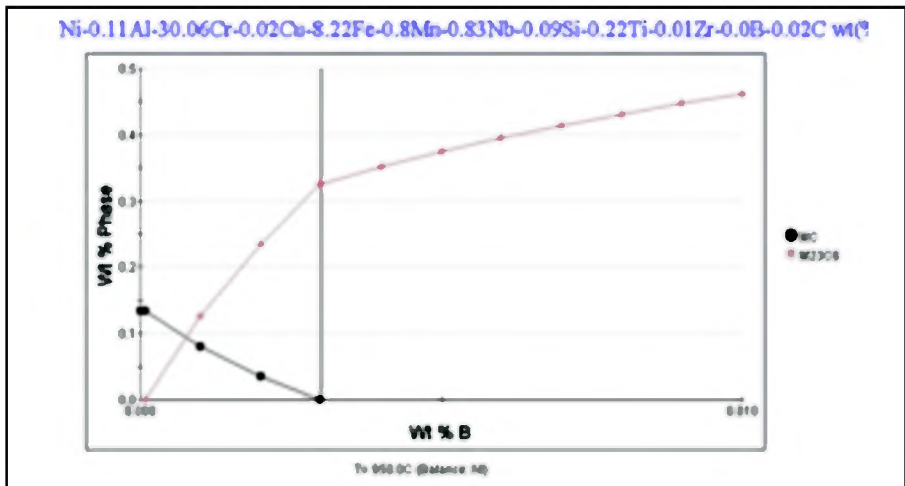


Fig. 6—Effect of boron content (0 to 0.01 wt-%) on equilibrium carbide stability in material B at 950°C. The nominal boron composition of material B is marked as a vertical line at 0.003 wt-%.

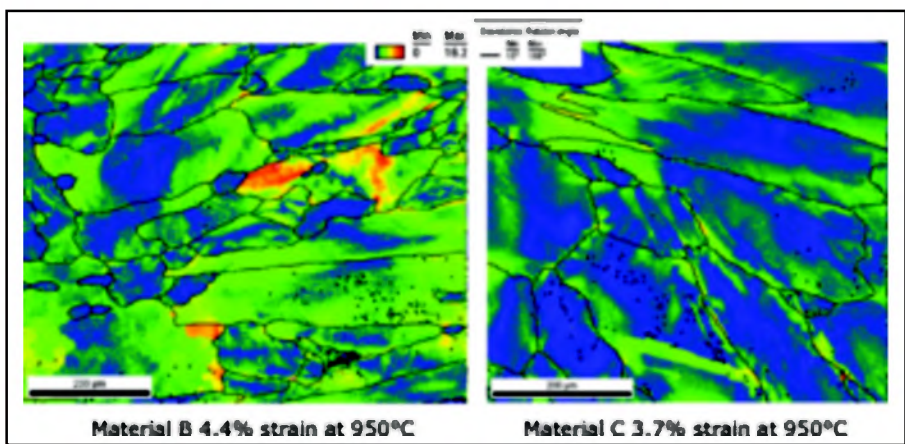


Fig. 7—Grain reference orientation deviation plot of EBSD scan of materials B and C after STF test at 950°C. Blue indicates point with an orientation close to the average orientation of that particular grain while yellow and red indicate greater crystallographic deviation. The black lines represent high-angle ($>10^\circ$) grain boundaries.

tability. EDS was used for qualitative chemical analysis of the carbides in these alloys and those results were compared with the analysis of similar alloys completed previously (Ref. 26). The results of the carbide analysis from the microstructural characterization of materials B, C, and H are summarized in Table 2 along with the thermodynamic solidification and equilibrium JMatPro-Ni calculations (Ref. 5).

In the as-welded condition, electron microscopy of materials B and C revealed 0.5 to 1 μm Nb- and Ti-rich M(C,N) intragranular carbides that were sparsely dispersed through the microstructure. These intragranular carbides were not typically observed pinning grain boundaries as their size and distribution were inadequate to have a significant effect on the boundary migration at elevated temperatures — Figs. 3A and 4A. Cr-rich M₂₃C₆-type intergranular carbides were observed

on the majority of grain boundaries in material B but the grain boundaries in material C were clean and practically free of carbides in the as-welded condition — Figs. 3B and 4B. In material B, the intergranular carbides were $<0.5 \mu\text{m}$ in size and while carbides were observed on the majority of boundaries, the number of carbides varied from boundary to boundary and some of the boundaries remained free of carbides.

The as-welded microstructure of material H contained numerous larger 1- to 5- μm M(C,N) carbides that form along the solidification grain boundaries at the end of solidification and were found to be effective at pinning migrated grain boundaries — Fig. 5B. The morphology of some of the interdendritic carbides were difficult to characterize as the particles had a skeletal structure and were often composed of groups of smaller carbides agglomerated together (Ref. 5). JMatPro-

Ni calculations of phase stability in material H included Delta, Laves, and Sigma phases, which were noted on Table 2 as “predicted.” As these phases are Ni rich or Cr rich, they were difficult to distinguish from the gamma substrate with EDS and were therefore noted in Table 2 as “possible.” Intergranular M₂₃C₆ carbides were not observed along the grain boundaries of material H in the as-welded condition.

The microstructures of materials B, C, and H were then evaluated after STF testing at 950°C and approximately 1% strain. In all three materials, the larger intragranular M(C,N) carbides appeared unchanged in either size or distribution — Figs. 3C, 4C, and 5C. In materials B and C there was an increase in the number of chromium-rich M₂₃C₆-type carbides observed along grain boundaries after STF testing — Figs. 3D and 4D. Almost all of the boundaries in material B were decorated with the intergranular carbides with some of the carbides displaying a slightly elongated morphology. In material C, the distribution of intergranular carbides was not as consistent as in material B and some boundaries remained free of carbides. In material H, some M₂₃C₆ precipitation was observed (Fig. 5C) but these carbides were not as apparent as in materials B and C.

In both materials B and C, a significant number of new carbides precipitated on the grain boundaries when the samples were strained at temperature during STF testing. STF samples that were heated to 950°C, and not strained, precipitated significantly fewer new carbides. This distinction becomes important when evaluating strained samples or real multipass weldments for the presence of intergranular carbides as the carbides may not have been present prior to strain. In material B there were more intergranular carbides before STF testing and are believed to have provided resistance to boundary sliding, contributing to the improved DDC resistance observed in this alloy.

Boron is known to increase the thermodynamic phase stability and precipitation kinetics of M₂₃C₆ and boron segregation to grain boundaries likely contributed to the improved stability of M₂₃C₆ over MC in material B (Refs. 32, 33). JMatPro-Ni calculations of equilibrium phase stability for the material B composition with different boron levels is shown in Fig. 6 and is consistent with the microstructural observations for materials B and C. By “engineering” the boron- and carbide-forming elements in these alloys, an improvement in DDC resistance appears to be achievable through the controlled precipitation of M₂₃C₆ along migrated grain boundaries in the as-welded microstructure. To further investigate this effect, tests to alter the grain boundary carbides were designed using a combination of heat

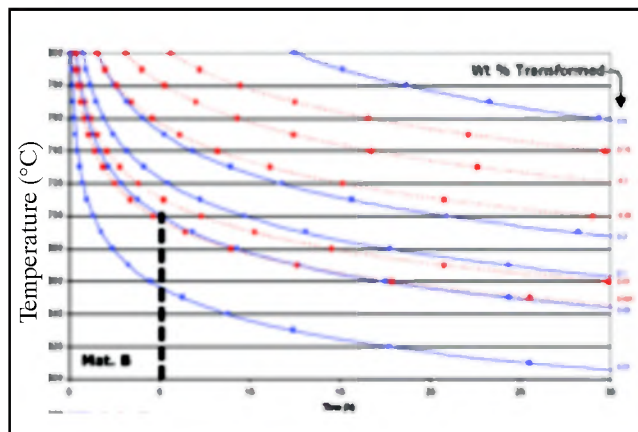
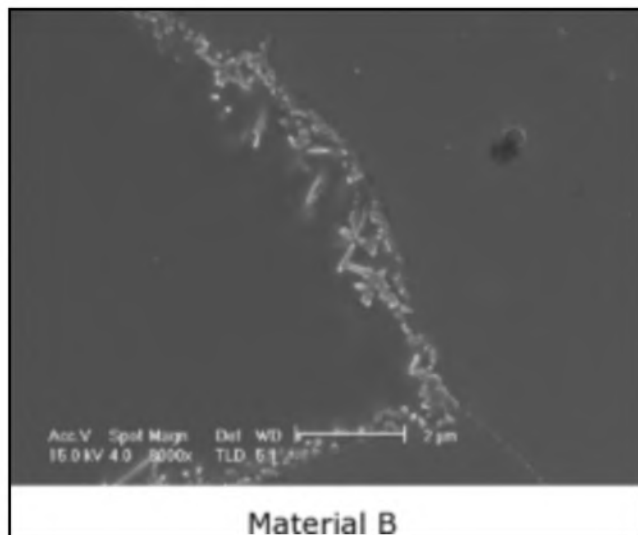
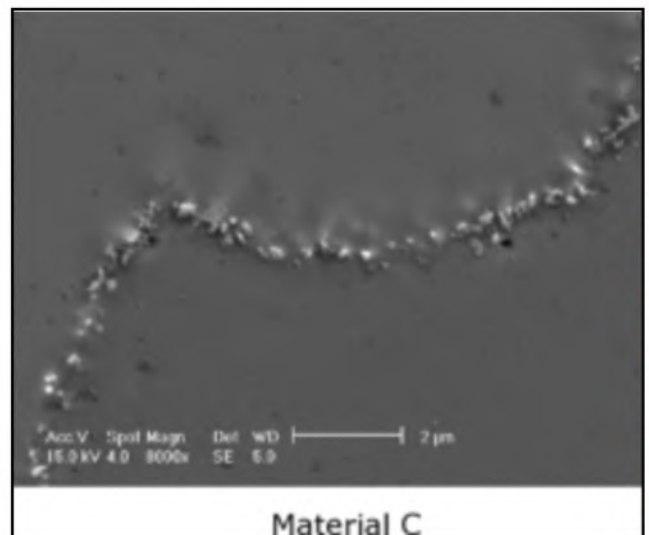


Fig. 8 — Series of overlaid TTT curves for materials B and C showing percent transformed for MC and $M_{23}C_6$ precipitates for different times and temperatures.



Material B



Material C

Fig. 9 — $M_{23}C_6$ carbide precipitation in materials B and C after a solutionizing heat treatment (1275°C for 1 min) followed by a precipitation heat treatment (700°C for 5 and 3.75 h, respectively).

treatment and controlled deformation.

Deformation

Carbide Engineering and Microscopic Boundary Pinning

To better understand how strain is accommodated within each material and how it is affected by the starting microstructure, EBSD scans of materials B and C were performed before and after STF testing (Ref. 5). EBSD GROD (grain reference orientation deviation) plots are developed using EBSD orientation data to evaluate the orientation relationship within a given grain. By calculating the average orientation within the grain and assigning a color gradient to graphically show deviations from that average orientation (0 deg blue, 4 deg green, 8 deg yellow, 12 deg orange, 16 deg red), a better understanding of how the grain is accommodating strain was obtained. For example,

if an area within a grain of a before-STF plot is blue and the same area of the after-STF plot is yellow, this area has the same relative misorientation and therefore deformed together. However, areas within a grain that were originally all blue, but after deformation now include a transition from blue to yellow, have presumably deformed at the location of the transition. Since most of the as-welded scans were primarily blue with 10–25% green (Ref. 5), misorientation transitions from blue to yellow or green to yellow in the after-STF scans can be assumed to be the result of deformation at the color transitions. It is important to remember that since the average orientation is recalculated for each grain (outlined with black lines that define >10-deg point-to-point misorientation), care should be taken when interpreting data between grains.

EBSD GROD plots in Fig. 7 were strained to 4% ($\pm 0.5\%$) and demonstrate the generally observed trend in materials B

and C that more misorientation transitions (i.e., blue to yellow) are located near grain boundaries in material C indicating more intergranular deformation while the transitions tended to occur more within the grains in material B indicating more intragranular deformation. There are still considerable deformation gradients within individual grains of B, but they are not as localized around grain boundaries or triple points as was found in C. Additional examples of strain effects using this technique are available elsewhere (Ref. 5).

Since grain boundary $M_{23}C_6$ carbides precipitated during STF testing for both materials B and C, the difference in deformation location appears to be controlled by the $M_{23}C_6$ carbides in material B that form in the as-welded condition (before testing). The presence of these carbides is believed to cause microscopic pinning of the grain boundaries, which thereby limits grain boundary sliding and promotes intragranular deformation.

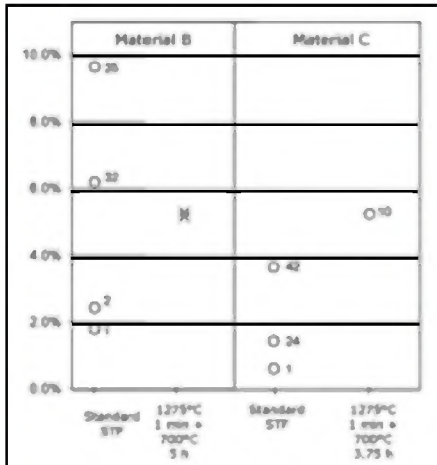


Fig. 10—STF results for materials B and C (12.7-s downslope) heat treated at several different conditions and compared with standard STF samples (results from Fig. 2). An “x” represents a tested sample with no DDC cracking and “o” a sample with DDC cracking. The number next to the circle is the number of DDC cracks found. The two blue “x” points in material B indicate samples that dynamically recrystallized during STF testing.

To better understand this microscopic pinning effect by grain boundary carbides, several heat treatments were devised to alter the carbide size and distribution. Samples were tested with combinations of solutionizing and precipitation heat treatments based upon JMatPro-Ni calculations (Ref. 5). Samples of materials B and C in the as-welded condition where solution heat treated in a protective argon environment at 1275°C for 1 min to dissolve most of the carbides and then allowed to free cool (approximately 30°C/s to 1000°C and 20°C/s from 1000° to 800°C) to room temperature. The peak temperature of 1275°C was selected as it was approximately 50°C below the melting temperature of both materials B and C. Based upon several trials, a hold time of 1 min maximized the amount of MC-type carbides that dissolved without significantly affecting the grain structure. Following this heat treatment, both materials were found to have a few small (<1 μm) MN-type precipitates remaining. Consistent with the as-welded microstructures, sporadic M₂₃C₆ carbides formed during cooling along grain boundaries in material B but not in material C.

Following the initial solution heat treatment, samples of materials B and C were given subsequent precipitation heat treatments at 700°C for times of 5 and 3.75 h, respectively, to precipitate approximately 0.05 wt-% M₂₃C₆ based upon JMatPro-Ni TTT calculations shown in Fig. 8. Following the precipitation heat treatment, M₂₃C₆ carbides were found along grain boundaries (Fig. 9) with a greater density than observed in the standard as-welded samples — Figs. 3B and 4B. However,

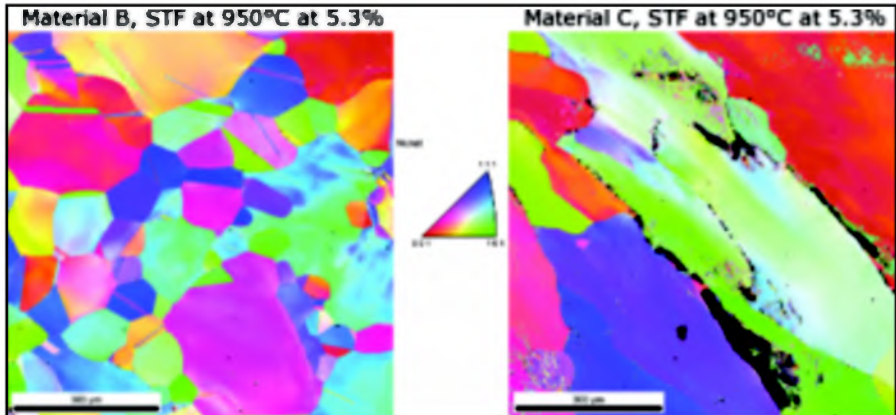


Fig. 11—Inverse pole figure plots of EBSD data showing samples of materials B and C that had been (precipitation) heat treated and STF tested at 950°C. The recrystallized microstructure in material B had smaller grains and three (60-deg) twin boundaries throughout the structure.

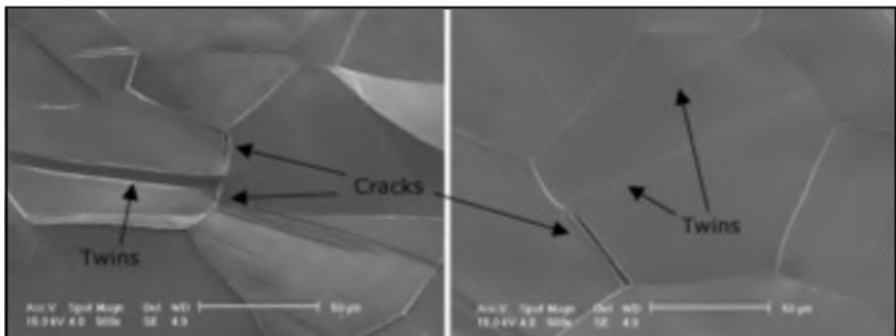


Fig. 12—SEM image of the surface of an as-tested, dynamically recrystallized material B sample tested at 950°C and 5.3% strain where small cracks formed along the grain boundary between a triple point and a twin boundary.

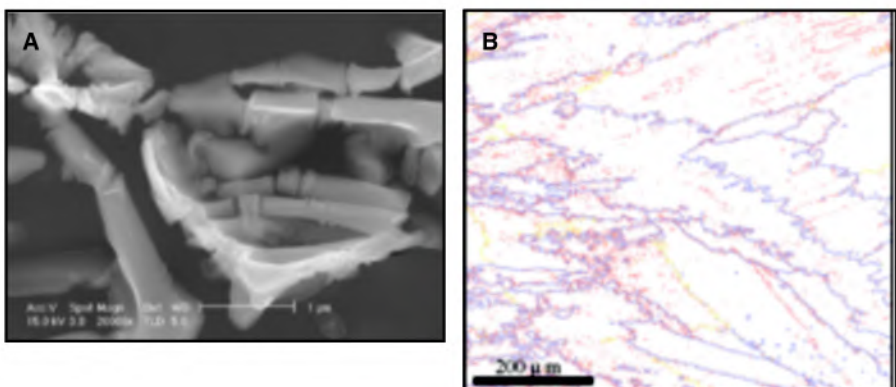


Fig. 13—SEM image of a skeletal carbide (A) found in material H and a grain boundary map from EBSD data showing the tortuous boundaries that result (B). The 2- to 15-deg boundaries are displayed red, 15- to 55-deg and 65- to 180-deg boundaries are blue, and 55- to 65-deg boundaries are yellow.

some of the boundaries remained relatively carbide free (<10% in material B and ~50% in material C) even after the heat treatment. The carbides in material B were generally elongated while those in material C were more symmetrical.

Subsequent STF testing of the heat-treated samples resulted in an increase in the cracking resistance of both materials B and C — Fig. 10. The STF results of material C in the precipitation heat-treated condition are similar to material B in the standard as-welded STF condition. The

similarity between the grain boundary carbide distributions of these two microstructures before STF testing is in good agreement with the STF results and the microscopic boundary sliding mechanism. However, it is unclear to what extent this mechanism could be used in welds as the grain boundary carbides in these alloys become thermodynamically unstable above approximately 1100°C (Ref. 5). The kinetics of formation, therefore, becomes important in multipass welds where thermal cycles are relatively short and time to re-

form these carbides is limited.

As discussed earlier, boron plays a key role in the kinetics of dissolution and formation of the $M_{23}C_6$ boundary carbides and was found to have an effect on the DDC susceptibility in the alloys studied in this work (Ref. 1). In the materials evaluated in Part 1, increases in boron lead to an increase in the transition to gross cracking and based on the microstructure analysis of material B and C is related to the accelerated formation of intergranular $M_{23}C_6$. However, the effect that bulk composition has on the formation of different types, sizes, and morphologies of carbides and their subsequent effects on DDC in these alloys is complex and care should be taken to avoid an overly simplistic view of the boron effect. Additional work is required to further investigate the effect of boron and its interaction with other elements in these and other alloy systems (Ref. 5).

Recrystallization

The decrease in the number of cracks in the precipitation heat-treated material B samples was also accompanied by recrystallization in the spot weld during STF testing at 950°C and approximately 5% strain — Fig. 11. The recrystallization is believed to have resulted from particle-stimulated nucleation (PSN) as a result of the distribution of the elongated $M_{23}C_6$ carbides along the boundaries. To date, no other FM-52M-like alloys have recrystallized during STF testing at 950°C and while PSN is typically observed with larger precipitates ($>1\ \mu m$) (Refs. 34, 35), the manner in which the $M_{23}C_6$ carbides clustered (Fig. 9) together may have reduced the critical particle size for PSN to occur (Refs. 34, 35). While no cracks were found after STF testing using the standard optical approach at 30 \times magnification and therefore reported as no cracking in Fig. 10, several small cracks ($<50\ \mu m$) were observed along grain boundaries in the SEM — Fig. 12. When the material dynamically recrystallized, some of the new grain boundaries that formed would have been carbide free and therefore more susceptible to DDC. Any subsequent strain would lead to a DDC response similar to material C, which was relatively free of intergranular carbides in the as-welded condition. However, the resulting recrystallized microstructure formed $\Sigma 3$ twin boundaries that were found to blunt subsequent DDC crack propagation — Fig. 12. This observation of crack blunting by twin boundaries is consistent with previous results (Refs. 29, 36).

Macroscopic Boundary Pinning

STF testing of material H revealed a significant resistance to DDC without the

presence of $M_{23}C_6$ precipitates on grain boundaries — Fig. 2. This high resistance to DDC was attributed to the larger 1 to 5 μm skeletal carbides located throughout the microstructure. The dense distribution and large surface area of these carbides were highly effective at pinning boundaries, resulting in extremely irregular or “tortuous” boundaries — Fig. 13. This macroscopic boundary pinning has been reported previously in FM-82 alloys, although to a lesser extent (Refs. 11, 24) and acts to mechanically lock the boundaries and improves the DDC resistance by promoting intragranular deformation rather than grain boundary sliding. The macroscopic boundary locking in material H has been the most effective method for improving the DDC resistance in these FM-52M-like alloys.

Summary

The results of this work have led to the following observations regarding the effect of microstructure on DDC. Macroscopic grain boundary locking occurs when interdendritic carbides are effective at pinning grain boundaries during solidification and the resulting tortuous boundaries improve resistance by mechanical locking boundaries, resisting grain boundary sliding and subsequent DDC cracking. When strain is applied to these interlocked grains, boundary sliding becomes much more difficult due to the various boundary geometries (Fig. 13B), resulting in an increase in intragranular deformation. The effectiveness of these carbides decreases as their size, surface area, and density decrease. It should be noted that this mechanism does not improve the actual boundary strength but increases the strain required for cracking at grain boundaries (Refs. 28, 37). To date, the compositional modifications to Filler Metal 52 in material H (2.5% Nb and 4% Mo) and the resulting macroscopic grain boundary locking have been the most effective method for improving the DDC resistance in these FM-52M-type alloys.

Samples with grain boundary $M_{23}C_6$ carbides that formed before STF testing were more resistant to cracking when compared to samples that were free of grain boundary carbides. This appears to be due to microscopic grain boundary locking where the presence of carbides along the boundary increases the resistance to grain boundary sliding, leading to increased intragranular deformation. Even a moderate number of these carbides in the as-welded condition appears to increase the cracking resistance and may be sufficient in some applications where overall weld restraint is low. Since these intergranular carbides form in the solid state and often appear only after straining at temperature, their presence in

a cracked sample may not indicate they formed before cracking or were beneficial in any way. The effectiveness of this mechanism is largely dependant upon the carbide dissolution and precipitation kinetics. Boron appears to be effective in this regard by increasing the stability of the carbides and may also contribute to the observed elongated morphology that was observed in material B. While not as effective as the macroscopic boundary locking mechanism, alloy optimization through this mechanism may be useful in applications where heat-to-heat composition variations produce inconsistent DDC results and even a small increase in DDC resistance (1–2% strain) may be sufficient to avoid cracking.

Certain carbide distribution and morphologies could lead to recrystallization by PSN (Refs. 34, 35, 38) resulting in a smaller grain size, dislocation annihilation, and $\Sigma 3$ twin boundaries; all of these increase the resistance to cracking. Even if complete recrystallization does not occur, partial recrystallization (the formation of some new grains along previous grain boundaries) would effectively break up the continuous crack path and improve resistance by eliminating long and straight boundaries. The effectiveness of these observations appears to be directly related to the quantity and morphology of the intergranular carbides. It has been proposed that the onset of ductility recovery at the higher temperature range of the ductility-dip temperature range is the result of recrystallization (Refs. 6, 9–11, 39). These PSN recrystallization results are consistent with the increased DDC resistance in those observations, that is, recrystallization results in an increase in ductility. However, in the case of PSN in Alloy B, recrystallization will only occur one time as the precipitates along the grain boundary that are required for PSN, only formed with an extended heat treatment. Further work is required to determine if the PSN mechanism may be reduced to practice as no filler metal compositions tested to date have produced the required grain boundary carbides in the as-welded condition.

The increase in the DDC resistance observed in material B appears to be related to the precipitation of $M_{23}C_6$ carbides in the as-welded condition — Fig. 3B. There is no evidence of a deleterious effect that may be caused by the subsequent precipitation of intergranular carbides that precipitate during straining — Fig. 3D. As such, the results of this work support a mechanism for DDC in these alloys that is associated with grain boundary sliding and the ability of intergranular $M_{23}C_6$ carbides to resist sliding, as opposed to the precipitation-induced cracking mechanism proposed by Young et al. (Ref. 8).

Conclusions

The results of this work have led to the following conclusions regarding the mechanisms that affect susceptibility to ductility dip cracking (DDC) in high-chromium Ni-based alloys.

1. Microscopic grain boundary pinning by intergranular carbides improved DDC resistance in the STF test when the carbides are present along migrated grain boundaries in the weld metal prior to the application of the strain.

2. Macroscopic grain boundary pinning by MC carbides that form at the end of solidification was found to prevent the migration of grain boundaries and resulted in tortuous boundaries that significantly improve resistance to DDC.

3. Precipitate engineering via heat treatment resulted in dynamic recrystallization by PSN and $\Sigma 3$ twin boundary formation that improve the resistance to DDC.

4. DDC is an elevated-temperature grain boundary sliding mechanism. Such sliding can be opposed macroscopically by the formation of tortuous grain boundaries via a grain boundary pinning mechanism. Grain boundary sliding can also be reduced by the formation of grain boundary carbides in the solid state through appropriate alloying or by heat treatment.

Acknowledgments

The authors would like to thank Sam Kiser of Special Metals Welding Products Company (SMWPC), Dr. Suresh Babu of The Ohio State University, Dr. Morgan Gallagher (now with Acute Technologies, Inc.), Kenny Izor (now with Pratt and Whitney), and Dr. Ray Unocic from The Ohio State University for their assistance and insight during the course of this investigation. Thanks also to SMWPC for supplying filler metals and sample blanks used in some of the testing. Partial financial support for the project was provided by BWXT, Inc.

References

- Nissley, N. E., and Lippold, J. C. 2008. Ductility-dip cracking susceptibility of nickel-based weld metals, Part 1: Strain-to-fracture testing. *Welding Journal* 87(10): 257-s to 264-s.
- Nishimoto, K., Mori, H., and Hongoh, S. 1999. Effect of sulfur and thermal cycles on reheat cracking susceptibility in multi-pass weld metal of Fe-36% Ni alloy. IIW Doc. IX-1934-99.
- Nishimoto, K., Saida, K., and Okauchi, H. 2006. Microcracking in multipass weld metal of Alloy 690, Part 1 – Microcracking susceptibility in reheated weld metal. *Science and Technology of Welding and Joining* 11(4): 455–461.
- Lippold, J. C., and Ramirez, A. J. 2004. Insight into the mechanism of ductility dip cracking. IIW-IX-2123-04. Osaka, Japan.
- Nissley, N. E. 2006. Intermediate temperature grain boundary embrittlement in nickel-base weld metals. *Welding Engineering*. The Ohio State University: Columbus, Ohio. p. 204, www.ohiolink.edu/etd/view.cgi?acc_num=osu1156949345.
- Zhang, Y. C., Nakagawa, H., and Matsuda, R. 1985. Weldability of Fe-36%Ni alloy (Report V). *Transactions of JWRI* 14(2): 119–124.
- Dix, A. W., and Savage, W. F. 1971. Factors influencing strain-age cracking in Inconel X-750. *Welding Journal* 50(6): 247-s to 252-s.
- Young, G. A., et al. 2008. The mechanism of ductility dip cracking in nickel-chromium alloys. *Welding Journal* 87(2): 13.
- Nissley, N. E. 2002. Development of the strain-to-fracture test to study ductility-dip cracking in austenitic alloys. *Welding Engineering*. The Ohio State University: Columbus, Ohio, p. 104.
- Rhines, F. N., and Wray, P. J. 1961. Investigation of the intermediate temperature ductility minimum in metals. *Transactions of the ASM* 54: 117–128.
- Ramirez, A. J., and Lippold, J. C. 2004. High temperature behavior of Ni-base weld metal. II. Insight into the mechanism for ductility dip cracking. *Materials Science & Engineering A* 380(1–2).
- Ramirez, A. J., and Lippold, J. C. 2004. New insight into the mechanism of ductility dip cracking in Ni-base weld metals. *1st International Workshop, Hot Cracking Phenomena in Welds*. Springer-Verlag: Berlin, Germany. pp. 19–41.
- Haddrill, D. M., and Baker, R. G. 1965. Microcracking in austenitic weld metal. *British Welding Journal* 12(9).
- Zhang, Y. C., Nakagawa, H., and Matsuda, F. 1985. Weldability of Fe-36%Ni Alloy (Report VI). *Transactions of JWRI* 14(5): 125–134.
- Lin, W., and Cola, M. J. 1997. Weldability of Inconel filler metal 52. *78th American Welding Society Annual Meeting, Abstracts of Papers*. April 13–17, 1997. Los Angeles, Calif.
- Collins, M. G., and Lippold, J. C. 2003. An investigation of ductility dip cracking in nickel-based filler metals — Part I. *Welding Journal* 82(10): 288-s to 295-s.
- Collins, M. G., Lippold, J. C., and Kikel, J. M. 2003. Quantifying ductility-dip cracking susceptibility in nickel-base weld metals using the strain-to-fracture test. *6th International Conference: Trends in Welding Research*. Pine Mountain, Ga.: ASM. pp. 586–590.
- Nishimoto, K., et al. 2006. Microcracking in multipass weld metal of Alloy 690, Part 2 — Microcracking mechanism in reheated weld metal. *Science and Technology of Welding and Joining* 11(4): 462–470.
- Nishimoto, K., et al. 2006. Microcracking in multipass weld metal of Alloy 690, Part 3 – Prevention of microcracking in reheated weld metal by additions of La to filler metal. *Science and Technology of Welding and Joining* 11(4): 471–479.
- Capobianco, T. E., and Hanson, M. E. 2005. Auger spectroscopy results from ductility dip cracks opened under ultra-high vacuum. *7th International Conference: Trends in Welding Research*. Callaway Gardens Resort, Pine Mountain, Ga.: ASM International. pp. 767–772.
- Matsuda, F. 1984. Weldability of Fe — 36% Ni alloy. II. — Effect of chemical composition on reheated hot cracking in weld metal. *Trans. JWRI* 13(2): 241–247.
- Ramirez, A. J., Sowards, J. W., and Lippold, J. C. 2005. Effect of Nb and Ti on the ductility dip cracking of Ni-base alloys weld metal. *60th Annual ABM International Congress*. Belo Horizonte-MG, Brazil, July.
- Kikel, J. M., and Parker, D. M. 1998. Ductility dip cracking susceptibility of filler metal 52 and Alloy 690. *Trends in Welding Research*. June 1–5, 1998. Pine Mountain, Ga. pp. 757–762.
- Collins, M. G., Ramirez, A. J., and Lippold, J. C. 2004. An investigation of ductility-dip cracking in nickel-based weld metals — Part III. *Welding Journal* 83(2): 39-s to 49-s.
- Lippold, J. C., and Nissley, N. E. 2006. Further investigations of ductility-dip cracking in high chromium, ni-base filler metals. *59th Annual Assembly of the International Institute of Welding*. Quebec City, Canada.
- Ramirez, A. J., and Lippold, J. C. 2004. High temperature behavior of Ni-base weld metal. I. Ductility and microstructural characterization. *Materials Science & Engineering A* 380(1–2).
- Nissley, N. E., and Lippold, J. C. 2005. Ductility-dip cracking susceptibility of filler metal 52 and 52M Ni-base filler metals. *Proceedings of the 7th International Conference, Trends in Welding Research VII*. Pine Mountain, Ga.: ASM International. pp. 327–332.
- Lippold, J. C., and Nissley, N. E. 2008. Ductility dip cracking in high-Cr Ni-base filler metals. *Hot Cracking Phenomena in Welds II*, ISBN 978-3-540-78627-6: Springer. pp. 409–426.
- Dave, V. R., et al. 2004. Grain boundary character in Alloy 690 and ductility-dip cracking susceptibility. *Welding Journal* 83(1): 1-s to 5-s.
- Nissley, N. E., et al. 2002. Development of the strain-to-fracture test for evaluating ductility-dip cracking in austenitic stainless steels and Ni-base alloys. *Welding in the World* 46(7/8): 32–40.
- Gerhold, R. CEOF. 2006 cited; available from www.ceof.ohio-state.edu/.
- Richards, N. L., and Chaturvedi, M. C. 2000. Effect of minor elements on weldability of nickel base superalloys. *International Materials Reviews* 45(3): 109–129.
- Czyska-Filemonowicz, A., et al. 2003. The role of boron in the 9% chromium steels for steam power plants. *Parsons 2003: Sixth International Charles Parsons Turbine Conference*. Dublin, Ireland. pp. 365–377.
- Humphreys, F. J. 1977. The nucleation and recrystallization at second phase particles in deformed aluminum. *Acta Metallurgica* 24: pp. 1323–1344.
- Humphreys, F. J., and Hatherly, M. 2004. *Recrystallization and Related Annealing Phenomena*. 2nd ed. 2004, Amsterdam; Boston: Elsevier. 628 p.
- Qian, M., and Lippold, J. C. 2003. The effect of annealing twin-generated special grain boundaries on HAZ liquation cracking of nickel-base superalloys. *Acta Materialia* 51(12): 10.
- Lippold, J. C., and Nissley, N. E. 2007. Further investigations of ductility-dip cracking in high chromium, Ni-base filler metals. *Welding in the World* 51(9/10).
- Bay, B., and Hansen, N. 1979. Initial stages of recrystallization in aluminum of commercial purity. *Metallurgical Transactions A* 10A: 279–288.
- Collins, M. G. 2002. *An Investigation of Ductility Dip Cracking in Nickel-Base Filler Materials*. The Ohio State University, p. xix, 240 leaves.